

The Influence of Dust-Smoke Mixtures on Boundary Layer Processes and Nocturnal Warming in the Sahel

Christopher Phillips¹, Udaysankar Nair¹, Sundar Christopher¹

¹Atmospheric and Earth Science Department, University of Alabama in Huntsville, Huntsville Alabama, USA.

Corresponding author: Udaysankar Nair (nairu@uah.edu)

Key Points:

- Dust and smoke in combination cause nighttime warming if extinction due to smoke is less than half of total
- Near-surface air temperature response is non-monotonic during the daytime due to aerosol radiative forcing-PBL feedbacks
- Aerosols may be a substantial source of nocturnal warming during periods of enhanced land degradation and aridation

This article has been accepted for publication and undergone full peer review but has not been through the copyediting, typesetting, pagination and proofreading process, which may lead to differences between this version and the [Version of Record](#). Please cite this article as doi: [10.1029/2021JD036349](https://doi.org/10.1029/2021JD036349).

This article is protected by copyright. All rights reserved.

Abstract

Using a single column model with ground-based, aircraft, and satellite data sets we assess the combined role of smoke and dust aerosols, land degradation/aridization (LDA), and their impact on the planetary boundary layer (PBL) in influencing near-surface air temperature over the Sahel. Our study is unique because it assesses the combined role of smoke and dust aerosols on PBL evolution and near-surface air temperatures during both day and nighttime. More importantly, using a theoretical framework, we provide a careful explanation of the geophysical processes responsible for the changes in PBL and near-surface air temperature. Our results indicate that during northern hemisphere winter months, dust and smoke over Sahel radiatively combine to impact the PBL. We show that aerosol mixtures dominated by dust modify PBL height in a manner that minimizes/maximizes surface layer cooling/warming at times when daytime maximum/nocturnal minimum temperatures occur. Furthermore, we find that increasing smoke contribution to total column aerosol optical extinction counteracts nighttime warming through daytime cooling. When smoke constitutes half or more of the total column aerosol optical extinction, the ratio of longwave to shortwave radiative forcing is less than 10%, and nighttime cooling ensues. Minimum temperature is most sensitive to changes in mid-visible aerosol optical depth (AOD) values < 1 and doubling of dust AOD within this range during the 1950-1980 Sahelian LDA event is estimated to have a nocturnal warming potential of $0.6\text{ }^{\circ}\text{C}$.

Plain Language Summary

We use a weather model to investigate how dust and smoke from agricultural fires impact the near-surface air temperature of Sahel. As vegetation in the region is reduced due to drought and expansion of the Sahara, it is expected that more dusty days will occur. We find that so long as dust dominates over smoke, increasing the concentration of dust and smoke causes daytime cooling but nighttime warming compared to days without smoke and dust. The nighttime warming is caused by large dust particles that trap heat escaping from Earth's surface, while daytime cooling is due to shade produced by smoke and dust. Stagnant conditions near the surface at night concentrate the heat in a shallow layer, enhancing warming. When smoke dominates, however, both day and nighttime are cooler since dust cannot trap enough heat to offset the daytime shading. Importantly, shading during the daytime also increases stagnation at the surface during nighttime. This enhances nighttime cooling due to a thinner near-surface layer and reduces mixing of warm air from aloft due to the increased stagnation. Through these mechanisms continued reduction of vegetation in the Sahel will lead to more warm nights, a result similar to greenhouse gas warming.

1 Introduction

Sahel and other dryland regions around the globe have experienced 20-40% more surface warming than humid regions (Huang et al., 2017; Zhou, 2016), driven by both global and regional forcing. Increases in greenhouse gasses (GHG) enhance downwelling radiation at the surface and disproportionately affect nighttime temperature when air is confined to a shallow nocturnal boundary layer (NBL) (Andrews et al., 2009; Zhou et al., 2010). This asymmetric warming is thus associated with GHG-induced climate change (IPCC, 2021; Rohde et al., 2013). However, land degradation and aridization (LDA), such as occurred in Sahel during the prolonged drought of 1950-1980, duplicate this warming signal. LDA reduce soil organic matter, leaf area, leaf water, soil moisture, and surface emissivity, thereby decreasing surface energy loss through upwelling longwave radiation (Zhou et al., 2007, 2008). The loss of vegetation cover also reduces shading and increases energy stored in the soil layer during daytime. The excess accumulated energy is then transferred to the atmosphere during nighttime. Subsequent warming is further amplified by the shallow NBL.

Similar to GHGs, atmospheric aerosols such as dust increase downwelling longwave radiation at the surface, increasing near-surface air temperatures during the night (Nair et al., 2011; Slingo, White, et al., 2009; Tsikerdekis et al., 2019). They also modulate shortwave radiation during the day (Slingo, White, et al., 2009), lowering daytime temperatures. This effect varies with aerosol size/composition, vertical distribution, and total column loading (Johnson, Heese, et al., 2008; Meloni et al., 2015). This is especially interesting in the northern hemisphere winter months when both smoke aerosols with sub-micron sizes and dust aerosols with larger particle sizes affect the diurnal variation of near-surface air temperatures (Gkikas et al., 2018; Heinold et al., 2011). The potential for the dust aerosols to cause surface warming is largely confined to nighttime and realized only if downwelling longwave aerosol radiative forcing at the surface is sufficient to offset daytime cooling due to increased reflectivity from both smoke and dust aerosols. The near-surface temperature sensitivity to aerosol radiative forcing, however, depends strongly on the properties of the surface such as albedo, emissivity, and soil moisture with arid regions like Sahel displaying greater sensitivity to aerosol radiative forcing than other regions (Chakraborty & Lee, 2019; Wei et al., 2021). Further, near-surface air temperature response to aerosol radiative forcing is modulated by planetary boundary layer (PBL) evolution. However, PBL evolution itself is modified by aerosol forcing (Li et al., 2017; Lou et al., 2019), and how this coupled process modulates nighttime warming potential of aerosols is not well understood.

Over Sahel, dust is the dominant aerosol and is known to have nighttime warming potential (Hansell et al., 2010; Nair et al., 2011; Tsikerdekis et al., 2019). Further, North Africa is estimated to emit over half of total atmospheric dust worldwide with Sahel being a focal point of emissions (Engelstaedter et al., 2003; Ginoux et al., 2001; Tanaka & Chiba, 2006). These dust aerosols are transported into the North Atlantic, even as far as the Gulf of Mexico (Gama et al., 2015; Prospero & Mayol-Bracero, 2013), and increase total column albedo, decrease daytime surface temperature, and reduce monsoon rainfall over Sahel (Gkikas et al., 2018; Lau & Kim, 2007; Tsikerdekis et al., 2019; Yoshioka et al., 2007). However, dust emission is influenced by anthropogenic and natural climate forcing, including LDA. The atmospheric dust loading over the northern tropical Atlantic, downwind of Sahel, more than doubled during the 1950-1980 LDA event over Sahel (Evan & Mukhopadhyay, 2010). Additionally, biomass burning aerosols, i.e. smoke, are released during agricultural burning events during the dry season and create plumes that extend across Sahel mixing with dust emissions (Johnson, Osborne, et al., 2008; Pinker et al., 2010; Van Der Werf et al., 2006). These plumes are also transported into the Atlantic where they reduce sea surface temperature, induce atmospheric heating, and potentially change the timing of the West African Monsoon (Solmon et al., 2021).

Previous research has done much work investigating the effects of the land surface and aerosols on regional and global climates, finding that arid regions are more susceptible to aerosol radiative forcing with consequences for surface temperature and precipitation distribution. However, the change in radiative forcing for varying combinations of smoke and dust and their feedback with PBL evolution have received less attention. In this study we use observationally constrained single column modeling (SCM) to assess the following issues: 1) how do biomass burning aerosols and boundary layer evolution modulate the surface thermal response to dust radiative forcing? 2) are mixtures of dust and smoke typically found over Sahel capable of causing nighttime warming? 3) could added atmospheric dust loading during events like the 1950-1980 Sahel LDA event complement nocturnal warming caused by land surface changes?

2 Materials and Methods

2.1 Single Column Modeling Experiments

Unlike prior studies that utilize three-dimensional numerical models (e.g. Tuccella et al, 2020), we use SCM sensitivity analysis to conduct systematic investigations of aerosol loading and composition effects on near-surface air

temperature. Use of the SCM allows a parameter space experimental approach that considers multiple combinations of aerosol loading, dust-smoke mixtures, and initial atmospheric conditions. While confined to cloud-free and synoptically quiescent conditions, the parameter space approach utilized is designed to enable: 1) theoretical analysis of coupling between aerosol radiative forcing, boundary layer evolution and land-atmosphere interactions and; 2) linking near-surface air temperature response to aerosol-radiative forcing in models to corresponding observed behavior through statistical modeling. We use the SCM configuration of the Weather Research and Forecasting Chemistry model (hereafter WRFSCM) (Chin et al., 2002; Skamarock et al., 2008) with the parameterizations listed in Table 1 for conducting the experiments. Note that, consistent with assumption of clear sky and quiescent synoptic conditions, microphysics parameterization is not activated, and externally specified advective forcing is imposed. The WRFSCM uses two grid cells in the x and y directions. Horizontal homogeneity is specified through the use of periodic lateral boundary conditions. A horizontal grid spacing of 4 km is used to avoid explicitly resolving convective eddies. Sixty sigma levels are prescribed between the surface and 18km with the first twenty-one levels contained below 2km and the first model level at 57 m above the surface. A 24-hour model spin-up period is used and analysis focuses on the second diurnal cycle of the experiment. While our approach is effective for conceptual analysis, limitations include the assumption of clear sky and synoptically quiescent conditions and the absence of large-scale coupling effects. We address these limitations in section 3.4 using statistical analysis of observations.

For the parameter space study, twenty four case study days and spread throughout the year 2006 are selected based on minimal cloud cover (< 20% peak cloud fraction in ARM observations). The study period is limited to 2006 due to availability of ARM observations in the study region. Boundary layer evolution for a forty-eight hour period was simulated using the WRFSCM for the selected case days (Table 2) in the following scenarios. The *control experiments* consisted of simulations where the aerosol vertical distribution, column loading, and dust to smoke proportions were specified using observational constraints as discussed in section 2.3. . *Aerosol free experiments*, identical to the control experiments but with zero AOD, were conducted to examine aerosol impact on near-surface air temperature. Both the control and aerosol free experiments are then repeated in the *model resolution experiments*, to determine the influence of model vertical resolution on the investigated PBL-aerosol interactions. The model resolution experiments use a grid spacing of 50km and only 18 levels in the vertical for WRFSCM, similar to other dust studies using coarse-grid modeling (Tsikerdekis et al., 2019). Additionally, since aircraft measured aerosol vertical profiles were confined to

January and February of 2006, we tested the sensitivity of WRFSCM to seasonal variations in aerosol vertical distribution through *vertical distribution experiments*. In the vertical distribution experiments, control experiments were repeated using Cloud-Aerosol Lidar and Infrared Pathfinder Satellite Observation (CALIPSO) derived average vertical distributions of smoke and dust aerosols during the spring, summer, fall, and winter seasons of 2007-2015. Lastly, for a subset of seven case days for which the control simulations showed good agreement with observations of surface meteorology and energy budget, the control experiments were repeated by systematically varying AOD and increasing proportion of dust from 0-2 and 0-1 respectively. These *aerosol sensitivity experiments* were used to assess whether the ranges of AOD and aerosol composition (dust/smoke combination) observed over Sahel increased the near-surface air temperature. Further, the aerosol sensitivity experiments are used to estimate the near-surface air temperature response to increased dust loading over Sahel during the 1950-1980 LDA event. Model experiments are summarized in Table 3.

2.2 Use of Observations to Initialize and Validate WRFSCM

We utilized radiosondes, surface meteorology, energy budget, and cloud observations from the ARM deployment in Niamey, Niger (13.5 ° N, 2.1 ° E) during the year 2006 (Miller & Slingo, 2007) to initialize and evaluate the SCM simulations. Each simulation was initialized using a rawinsonde profile from the Niamey, Niger Atmospheric Radiation Measurement (ARM) site near 0000 UTC (Keeler et al., 2006). The radiosondes measure temperature (± 0.5 ° C uncertainty), pressure (± 1.0 hPa uncertainty), and relative humidity ($\pm 5\%$ uncertainty). The initial conditions for each case vary but are characterized by strong surface-based inversions with an overlying mixed layer (example in Figure 1). Additionally, near-surface dewpoint depressions often exceed 20 ° C, indicating a dry atmosphere.

Aerosol vertical distribution was specified using aircraft observations (Haywood et al., 2008; Johnson, Heese, et al., 2008; Johnson, Osborne, et al., 2008), and proportional contributions of smoke and dust aerosols to column loading were parameterized using ground observations of aerosol optical depth (AOD) and Angstrom exponent (AE) from the Aerosol Robotic Network (AeRoNet) station in Banizoumbou, Niger (Dubovik et al., 2000; Holben et al., 1998; Tanre & Rajot, 2022). Twenty-four days in 2006 with minimal (<25%) cloud cover were considered in the SCM experiments to sample seasonal atmospheric and aerosols conditions from the AERONET station in Banizoumbou, Niger (mean

AOD = 0.53, inter-quartile range = 0.31; mean AE = 0.37, inter-quartile range = 0.34; Figure 2a). These days were selected by visible inspection of imagery from the AMF total sky imager which provides full hemisphere imagery of sky conditions (Miller & Slingo, 2007).

ARM surface meteorology (Kyrouac & Shi, 2005) and surface energy budget observations (Sengupta et al., 2005a, 2005b; Sullivan et al., 2005) are used to validate the WRF SCM Control simulations. Surface temperature, pressure, and humidity are measured by the ARM Mobile Facility (AMF) meteorological station (Miller & Slingo, 2007) and have uncertainties of $\pm 0.57^\circ\text{C}$, $\pm 0.04\text{ hPa}$, and $\pm 2.06\%$ respectively. Downwelling shortwave and longwave radiation are observed using a precision spectral pyranometer (PSP) ($\pm 4\%$) and precision infrared radiometer (PIR) ($\pm 5\% + 4\text{ W m}^{-2}$) radiometers with and uncertainty respectively. Upwelling shortwave and longwave radiation are measured using a PSP ($\pm 2\%$) and PIR ($\pm 2\%$) radiometers. Sensible and latent heat fluxes are measured using an eddy correlation flux measurement system (Sullivan et al., 2005) with 6% and 5% uncertainties respectively. Soil moisture is taken from ERA-Interim re-analysis (Berrisford et al., 2011).

2.3 Radiative Transfer and Parameterization of Aerosols

The Fu-Liou-Gu radiative transfer scheme (FLG-RS) (Gu et al., 2011), which allows for specification of radiative forcing of aerosols, is used in this study. Radiative forcing of aerosols are imposed by specifying the appropriate optical properties and vertical distribution of biomass burning and mineral dust aerosols that are typically present in the Sahel, including asymmetry parameter (g), single scattering albedo (ω_0), and extinction coefficient (β_{ext}). For the case days considered in the study, regular observations of aerosol optical depth (AOD), and Angstrom Exponent (AE) for the year 2006 are available from the AeRoNet (Dubovik et al., 2000; Holben et al., 1998). Optical properties are characterized using the Optical Properties of Aerosols and Clouds (OPAC) data base (Hess et al., 1998). The OPAC desert dust model is used to prescribe optical properties of dust aerosols. For biomass burning aerosols, optical characteristics are derived from OPAC using an aerosol mixture (Table 4) based on aircraft observations from the Dust and Biomass Burning experiment (Johnson, Heese, et al., 2008; Johnson, Osborne, et al., 2008). The aerosol hygroscopic effect is accounted for by using the OPAC software to compute β_{ext} , ω_0 , and g for dust and smoke as a function of wavelength (λ) for eight discrete relative humidity (RH) values spanning the range 0-100%. Furthermore, unlike previous studies (Curci et al., 2019; Formenti et al., 2011; Scarnato et al., 2015; Tuccella et al., 2020) we do

not consider the various mixing states of aerosols and ongoing chemistry since our study is focused on how bulk aerosol properties affect near-surface air temperature and the PBL.

To constrain vertical distribution of aerosols in WRFSCM, we use mean altitudinal profiles of smoke and dust aerosol extinction coefficient (β_{ext}) at 550nm wavelength derived from in-situ aircraft and ground based measurements made during the Dust and Biomass-Burning Aerosol Experiment (DABEX) field campaign (Haywood et al., 2008). Prior analysis of DABEX observations (Johnson, Heese, et al., 2008) found the following linear relationship between observed AE and the fractional contribution of biomass burning (f_{bb}) to total aerosol β_{ext} :

$$f_{bb} = 0.5866AE + 0.0047 \quad (1)$$

We utilize f_{bb} along with the assumption that the vertical variation of β_{ext} is solely due to variation in total number concentration to parameterize the optical depth for a model vertical layer as follows:

$$\tilde{\tau}_{\lambda}^n(z_1, z_2) = \frac{f_n \tau_{0.55}}{\tilde{\tau}_{0.55}^n} \int \tilde{\beta}_{ext}^n(\lambda) S^n(z) dz \quad (2)$$

where $\tilde{\tau}_{\lambda}^n(z_1, z_2)$ is the layer optical depth for species n (1 - dust, 2 - biomass burning), $\tau_{0.55}$ is the ARM observed total AOD for the selected case day, f_n is the fractional contribution of species n to total optical depth, $\tilde{\tau}_{0.55}^n$ is the optical depth for species n at 0.55 μm computed using profiles from DABEX (Haywood et al., 2008; Miller & Slingo, 2007), $\tilde{\beta}_{ext}^n(\lambda)$ is the OPAC estimated extinction coefficient (λ) for aerosol species n at wavelength λ , and $S^n(z)$ is the scaling factor given by the ratio $\beta_{ext}^n(0.55 \mu m, z) / \tilde{\beta}_{ext}^n(0.55 \mu m)$. Note that $\beta_{ext}^n(0.55 \mu m, z)$ is the vertical profile of the climatological extinction coefficient for species n . $f_1 = 1 - f_{bb}$ and $f_2 = f_{bb}$ for dust and smoke aerosols respectively. The value of f_{bb} is computed using equation (1) and the observed value of AE for the selected case days.

2.4 Statistical Modeling of Near-surface air temperature Response to Dust using Observations

We also conducted general linear regression modeling (GLM) analysis using surface meteorological observations from the ARM site in Niamey, Niger and AOD observations from the Banizoumbou, Niger AeRoNet station. In view of the restrictive assumptions of the WRFSCM (namely lack of advection and clouds), the GLM is used to validate behavior of temperature response to aerosols in the WRFSCM. The GLM initially considered season, AOD, T_{max} , cloud fraction (MODIS-derived), wind speed and direction, and water vapor mixing ratio at the time of occurrence of T_{min} as predictors of T_{min} . Wind speed and direction were also taken at the time of occurrence of T_{min} , and season

was modeled as a categorical variable with 1, 2, 3, and 4 representing winter (December, January, February), spring (March, April and May), summer (June, July and August) and fall (September, October and November), respectively. The optimal predictors were then selected using forward-backward stepwise regression modeling based on the Akaike Information Criterion (AIC) as described in Table 5 with the wind speed, wind direction, and cloud fraction variables being eliminated. We applied this statistical modeling approach ($r^2 = 0.85$) to surface observations during all months of 2006. Then using numerically simulated values of the predictor variables along with observed season and AOD, we used GLM to determine change in T_{\min} (ΔT_{\min}) as a function of AOD and compared this to the WRFSCM ΔT_{\min} for each case day.

3 Results and Discussion

We evaluated the veracity of the control experiments by comparing the simulated and observed surface meteorology/surface energy budget and found the performance of the WRFSCM to be comparable or superior to prior studies, despite the assumption of clear skies (Dimitrova et al., 2016; Kleczek et al., 2014; Sridhar et al., 2002; Sun et al., 2017). Mean Bias Error (MBE) of 2 m temperature is 0.31°C , and the Root Mean Square Error (RMSE) is 1.60°C . For sensible heat and latent heat fluxes, RMSE are 32.29 W m^{-2} and 7.81 W m^{-2} respectively. Sensible and latent heat flux MBE are 0.96 W m^{-2} and -2.52 W m^{-2} respectively. Downwelling shortwave radiation at the surface has a RMSE of 38.12 W m^{-2} and an MBE of -18.48 W m^{-2} . Surface downwelling longwave radiation RMSE is 12.88 W m^{-2} and, MBE is -2.52 W m^{-2} .

To compare trends in model surface meteorology, the case day of 17 March 2006 is examined (Figure 3). Model temperature (Figure 3a) is too warm during the early morning but quickly matches observations after dawn. Surface heat fluxes (Figure 3c) well-follow the observed trends, with latent heat flux particularly matching observations. This is expected given the dry conditions of Sahel. Crucially, the shortwave and longwave radiation in the model closely agree with observations (Figure 3d), illustrating that the radiative effects of aerosols are being sufficiently represented in the model. In the following sections we detail the results of the aerosol free experiments (section 3.1), the model resolution experiments (section 3.2), the aerosol sensitivity experiments (section 3.3), and the statistical analysis of observations (section 3.4).

3.1 Diurnal Variation of Surface Aerosol Radiative Forcing Impacts

We used the control and aerosol free experiments to assess the impact of aerosols on near-surface air temperature, boundary layer evolution, and surface energy budget (Figure 4). For observed combinations of dust ($\omega_0 = 0.95$) and smoke ($\omega_0 = 0.82$) at 550nm, due to increased reflectivity of aerosols, we find a mean decrease in downwelling shortwave radiation of 90-100 Wm^{-2} during the afternoon hours (Figure 4d). This is partially offset by increases in downwelling longwave radiation at the surface, which exceed 12 Wm^{-2} during all hours (Figure 4d). This reduction in solar radiation at the surface leads to daytime decreases in mean sensible heat flux of 40 Wm^{-2} . Furthermore, the increased longwave radiation from dust aerosols provides nighttime increases in sensible heat flux of 2 Wm^{-2} (Figure 4c). Mean daytime decrease in PBL height exceeds 600m, and NBL height increases by more than 25m (Figure 4b). The shortwave and longwave aerosol radiative forcing at the surface found here is within the range found in prior numerical modeling studies in the Sahel region (Chaibou et al., 2020; Huang et al., 2009; Patadia et al., 2009; Tsikerdekis et al., 2019; Yoshioka et al., 2007).

Daytime near-surface air temperature shows a complex, non-monotonic response (Figure 4a), with aerosol-driven daytime cooling with maximum values in the early morning hours (-1.1°C at ~ 7 UTC) and minimum values (-0.14°C) during the late afternoon hours when maximum air temperatures (T_{\max}) occur. However, during the nighttime aerosol forcing causes a monotonic warming response which is maximum (0.73°C) at the time of occurrence of the minimum temperature (T_{\min}). We tested the sensitivity of our results to aerosol vertical distribution (Figures 2b-e) by using the vertical distribution experiments. We found the results to remain statistically significant, but with higher daytime cooling and slightly reduced nocturnal warming (Table 6).

The complex time-varying near-surface air temperature response to aerosol radiative forcing may be understood by considering the following expression for perturbation in surface layer temperature tendency $\left(\Delta \left(\frac{\partial \theta_v}{\partial t}\right)\right)$ due to aerosol forcing (derivation in Appendix A):

$$\Delta \left(\frac{\partial \theta_v}{\partial t}\right) = \frac{\overset{A}{1.25 H_{sc}}}{\rho C_p h_c} \left(\frac{\overset{B}{\tilde{\beta}} - \overset{C}{\tilde{\alpha}}}{1 + \alpha} \right) \quad (3)$$

where α is the fractional change in the control experiment PBL depth and $\tilde{\alpha}$ is the fractional change in the control experiment surface heat flux. θ_v , ρ , C_p , H_{sc} , and h_c are virtual potential temperature, air density, specific heat of air at

constant pressure, heat flux at the surface in the aerosol free experiments, and boundary layer depth in the aerosol free experiments respectively. Terms B and C of (3) account for temperature tendency perturbations due to changes in surface heat fluxes and PBL height induced by aerosol radiative forcing respectively.

We used mean values of heat flux and PBL heights from the control and aerosol free experiments to quantify the competing effects of surface heat flux (terms A and B) and PBL height (terms A and C) changes induced by aerosol forcing on diurnal variation of temperature tendency perturbation (Figure 5a).

During daytime aerosol radiative forcing reduces surface sensible heat fluxes, heat flux convergence, and negative temperature tendency in the boundary layer. Reduction in surface sensible heat flux, however, is accompanied by diminished PBL height, thus increasing flux convergence and positive temperature tendencies within the boundary layer. Early in the day, the effect of fractional changes in heat fluxes dominates, producing maximum cooling. As the day advances, increases in PBL height progressively mitigate the cooling tendency due to reduced sensible heat fluxes.

Therefore, daytime temperature response to aerosol radiative forcing is minimized during the time period of T_{\max} . This process is illustrated conceptually in figures 5b and 5c.

Though some of the assumptions made to derive (3) are not strictly applicable to the NBL (namely the assumption of linear variation in heat flux with height; Appendix A), it is instructive to use (3) to analyze the impact of aerosol radiative forcing on NBL near-surface air temperature tendency. During nighttime, surface heat flux (H_s) is directed from the atmosphere to the ground ($H_s < 0$). Thus, the reduced magnitude of sensible heat flux due to aerosol radiative forcing (increased downwelling longwave radiation) reduces divergence of turbulent heat flux and produces warming within the NBL. Similarly, increases in NBL height caused by aerosol radiative forcing also decrease flux divergence and contribute to nocturnal warming. In contrast to the convective PBL, both terms B and C in (3) work in concert to produce a nearly monotonic warming tendency within the NBL (Figure 5a). Note that, while the NBL growth can entrain warm air from aloft and further counteracting nighttime cooling (McNider et al., 2012; Walters et al., 2007), this is absent from equation (3), and future work might consider it as a separate physical processes.

3.2 Effect of Model Vertical Resolution on Near-surface Air Temperature Response

In contrast to our original aerosol free experiment with 60 vertical levels, the model resolution experiments with only 18 levels show greatly reduced nocturnal warming, 0.43°C versus 0.73°C . This result is similar to previous work with a three-dimensional 18 layer numerical model (Tsikerdekis et al., 2019) that found mineral dust may increase T_{\min} by $0.1\text{-}0.3^{\circ}\text{C}$. Although it must be noted that Tsikerdekis et al. (2019) examined decadal influences of aerosols over Sahel, limiting direct comparison. The decrease in nocturnal warming observed in the 18 layer WRFSCM occurs despite a reduction in daytime cooling compared to the 60 level simulation (-0.07°C versus -0.14°C) and similar aerosol radiative forcing (Figure 6).

The greater discrepancy in nighttime warming than daytime cooling between the model simulations is likely due to the depth of the PBL in relation to the number of model grid points within that layer. During the daytime, both simulations show PBL depths exceeding 1 km across all case days. At this depth, the 18 level simulation has at least 6 grid points within the PBL, and the 60 level simulation has at least 15. Five to six grid points is considered adequate for resolution of a feature of interest (Warner, 2011), and thus the daytime discrepancy between the two simulations is fairly small (0.07°C during the daytime vs. 0.3°C at night). At nighttime, however, the PBL depth decreases to 200-250 m. The 18 level simulation has only 3 vertical levels within this height, while the 60 level simulation has 5. Three levels is certainly not sufficient to capture describe the aerosol-PBL feedback investigated in this study. Therefore, it is reasonable to conclude that the aerosol-boundary layer feedback described by equation (3) is not well-resolved within the more coarse simulations, particularly in the shallow NBL. Consequences of inadequately resolving aerosol-boundary layer coupling in coarse grid numerical models include: 1) underestimating mineral dust's contribution to surface warming and 2) not resolving the complex PBL temperature response to aerosol radiative forcing. Further work is required to quantify these effects however.

3.3 Influence of Aerosol Column Loading and Composition on Near-surface Air Temperature

We used the aerosol sensitivity WRFSCM experiments to construct a parameter space nomogram for examining the impact of both aerosol loading and composition on near-surface air temperature, namely T_{\max} , T_{\min} , and Diurnal Temperature Range (DTR) (Figure 7a). We found that T_{\min} increases with AOD provided that the proportional contribution of dust to aerosol extinction is greater than half. Within this region of positive T_{\min} forcing, sensitivity to AOD decreases both with increasing AOD and proportion of biomass burning aerosols (Figure 7b). Sensitivity of T_{\min}

to AOD is highest for AOD values less than ~ 1.0 . High sensitivity of DTR to AOD is also found within this range of AOD values, illustrating the dominant role of dust induced nighttime warming in DTR reduction (Figure 7b). As the proportion of smoke aerosols increases, however, sensitivity of DTR to AOD is dominated by the daytime cooling effect of aerosols. This behavior is tied to corresponding variability in proportions of longwave to shortwave radiative forcing (Figure 7c). For example, when AOD is 0.2, this ratio varies from ~ 0.25 to 0.1 as the dust proportion in the atmospheric column decreases from 1 to 0.5. For a fixed dust proportion, this ratio also decreases with increasing AOD, albeit over a smaller range (e.g. 0.25-0.23 for dust AOD of 0.0-2.0). Our analysis shows that this ratio must be $\sim 10\%$ or greater for longwave radiation to compensate for daytime cooling and produce nighttime warming. Surface observations show frequent occurrence of aerosols within the parameter space region that is conducive to surface warming (Figure 7d).

3.4 Statistical modeling of Near-surface Air Temperature Response to Dust using Observations

To validate conclusions drawn from the WRFSCM, we examine the influence of AOD on T_{\min} response in the GLM. This alleviates limitations of the WRFSCM, namely lack of cloud cover and large-scale coupling effects. While wind speed, wind direction, and cloud cover were initially considered in the GLM, these variables were found to be insignificant contributors to T_{\min} during the studied case days (section 2.4). Instead, season, daytime T_{\max} , near-surface water vapor mixing ratio, and AOD were bound to be the most influential predictors of T_{\min} (Table 5). Note that the statistical insignificance of the role of cloud cover on T_{\min} is consistent with prior analysis of cloud radiative forcing for the same time period used in this study (Bouniol et al., 2012; Slingo, White, et al., 2009). Bouniol et al. (2012) found the longwave radiative forcing at the surface to be small even during the monsoon season, when enhanced atmospheric moisture masked the surface effect of longwave cloud radiative forcing at the surface. Slingo et al. (2009) found atmospheric temperature and column water vapor to be negatively correlated, so that despite their variations, longwave divergence in the atmosphere showed little change throughout the year. Cloud cover is reduced during the dry season when dust is prevalent (Slingo, Bharmal, et al., 2009; Slingo, White, et al., 2009), and the dust layer itself is potentially masking the radiative effects of clouds. By averaging nighttime warming across all days, the GLM shows that after controlling for variations in T_{\max} and near-surface moisture, the presence of dust still induces nighttime warming (Figure 7e). The patterns of GLM and WRFSCM predicted T_{\min} response to aerosols are similar, but GLM predictions display greater warming, with T_{\min} sensitivity to AOD being 25-50% greater than in WRFSCM for AOD

0-2.0. Note that GLM performance is superior to the WRFSCM when comparing all case days (Figure 8). Thus, while WRFSCM is able to mimic the observed T_{\min} response to aerosols, it potentially underestimates nighttime warming. Inadequacies in surface layer parameterizations and representation of NBL dynamics that enhance warm air entrainment could be potential causes (Avolio et al., 2017; Kleczek et al., 2014; McNider et al., 2012; Walters et al., 2007) but further investigation is required. Despite differences in the magnitude of T_{\min} response to aerosols between the observational and modeling analysis, both the GLM and WRFSCM support the conclusion that dust aerosols can have a substantial warming effect on minimum temperatures.

4 Conclusions

We find that dust aerosol radiative forcing affects diurnal evolution of PBL in a manner that minimizes/maximizes the surface layer thermal response during the hours when maximum/minimum near-surface air temperatures tend to occur. While T_{\min} increases with dust optical depth, sensitivity of T_{\min} to changes in AOD decreases as AOD increases. For a given AOD, the ability of dust to cause nighttime warming decreases with increasing proportions of smoke and ceases when smoke fraction exceed 0.5. Alternatively, aerosol mixtures induced nighttime warming so long as downwelling longwave radiative forcing is $> 10\%$ of downwelling shortwave radiative forcing. T_{\min} sensitivity to aerosol radiative forcing is high for aerosol composition and AOD ranges typically found over Sahel. Similarly, AOD increase during the 1950-1980 LDA event also occurred within the range of AOD where T_{\min} sensitivity to aerosol radiative forcing is high. The increase in AOD during this period (0.3 to 0.7 on average) has the potential to complemented the nighttime warming due to land cover change by up to 0.6° C (Figure 7f).

Note that this study neglects the impact of aerosol mixing state on optical properties and radiative transfer computations (Formenti et al., 2011; Curci et al., 2019; Scarnato et al., 2015; Tuccella et al., 2020). While prior studies indicate dominant mode of mixing between dust and biomass burning to be external, up to a quarter of the aerosol mass could be composed of internally mixed particles with homogenous carbonaceous coating at surface of dust particles (Deboudt et al., 2010; Hand et al., 2010). Such mixing could result in increased absorption at short and longwave part of the spectrum. Additionally, soil types vary regionally and thus the dust optical properties do as well. These are some of the limitations that needs to be addressed by future work.

In the near future, LDA is expected to increase over drylands, which currently occupy 41% of global land area and house 38% of the human population (Huang et al., 2017). Thus, increased dust emissions could be expected to exacerbate disproportionate warming over drylands. In this context, inconsistent nighttime thermal response to dust radiative forcing in numerical models needs to be addressed.

Appendix A: Derivation of Temperature Perturbation Equation

To derive equation 3 begin with a form of the thermodynamic energy equation where advection is neglected:

$$\frac{\partial \theta_v}{\partial t} = \frac{-1}{\rho C_p} \frac{\partial F_{net}}{\partial z} - \frac{(\overline{\partial w' \theta'_v})}{\partial z}$$

where θ_v , R , C_p , ρ , F_{net} and $\overline{w' \theta'_v}$ are virtual potential temperature, gas constant, specific heat of air at constant pressure, air density, net flux of radiation, and turbulent flux of virtual potential temperature respectively. During daytime, vertical variation of virtual potential temperature flux $\overline{w' \theta'_v}$ scaled by value of eddy heat flux at the surface,

$(\overline{w' \theta'_v})_s$, varies linearly with height:

$$\frac{\overline{w' \theta'_v}}{(\overline{w' \theta'_v})_s} = 1 - 1.25 \left(\frac{z}{h} \right)$$

where h is the height of the boundary layer. This linear relationship has been found to hold for the mixed and surface layers, provided low wind shear conditions⁴⁰, a condition applicable to our simulated convective boundary layers.

Note that $H_s = \rho C_p (\overline{w' \theta'_v})_s$, where H_s and ρ are surface sensible heat flux (Wm^{-2}) and air density. Substituting for

$(\overline{w' \theta'_v})_s$ and then differentiating with respect to z yields the following relationship for the vertical divergence of virtual potential temperature flux:

$$\frac{-\partial (\overline{w' \theta'_v})}{\partial z} = 1.25 \left(\frac{H_s}{\rho C_p h} \right).$$

This equation may be applied across the mixed layer/surface layer boundary, as if heat flux is continuous between layers, then divergence of heat flux must be as well. At any time t , let the sensible heat fluxes and boundary layer heights for clear and dusty atmospheric conditions be H_{sc} , H_{sd} , and h_c , h_d respectively. Difference in vertical divergence

of virtual potential temperature flux $\left(\Delta \frac{\partial(\overline{w'\theta'_v})}{\partial z}\right)$ between dusty and clear conditions at any given time is then given

by:

$$-\left(\Delta \frac{\partial(\overline{w'\theta'_v})}{\partial z}\right) = \frac{1.25}{\rho C_p} \left(\frac{h_c H_{sd} - h_d H_{sc}}{h_d h_c}\right).$$

On the RHS of the thermodynamic energy equation, radiative flux divergence is substantially smaller compared to the divergence of turbulent fluxes. Defining $\Delta H_s = H_{sd} - H_{sc}$ and $\Delta h = h_d - h_c$ and neglecting the radiative flux divergence and difference in temperature tendency between the dusty and clear conditions, we find:

$$\Delta \left(\frac{\partial \theta_v}{\partial t}\right) = \frac{1.25}{\rho C_p} \frac{H_{sc}}{h_c \left(1 + \frac{\Delta h}{h_c}\right)} \left(\frac{\Delta H_s}{H_{sc}} - \frac{\Delta h}{h_c}\right)$$

With the substitutions of $\alpha = \Delta h/h_c$ and $\beta = \Delta H_s/H_{sc}$ we retrieve equation 3:

$$\Delta \left(\frac{\partial \theta_v}{\partial t}\right) = \frac{1.25 H_{sc}}{\rho C_p h_c} \left(\frac{\beta - \alpha}{1 + \alpha}\right)$$

Acknowledgments

The authors acknowledge financial support from the Alabama Graduate Research Scholars Program (GRSP) funded through the Alabama Commission for Higher Education and administered by the Alabama EPSCoR. Additionally, U. Nair is supported by the NSF CAREER program. Data were obtained through the Atmospheric Radiation Measurement (ARM) user facility, a U.S. Department of Energy (DOE) office of science user facility managed by the Office of Biological and Environmental Research. We also thank Didier Tanri and Jean Louis Rajot for their work in maintaining the Banizoumbou AeroNet site.

Open Research

The model used in this study is the Weather Research and Forecasting with Chemistry model version 3.7 (Skamarock et al., 2008) available at https://www2.mmm.ucar.edu/wrf/users/download/get_sources.html. ARM rawinsonde observations (Keeler et al., 2006) are available at <http://dx.doi.org/10.5439/1021460>, and the surface measurements (Kyrouac & Shi, 2005) are located at <http://dx.doi.org/10.5439/1786358>. AeRoNet AOD and AE

observations (Tanre & Rajot, 2022) are located at https://aeronet.gsfc.nasa.gov/cgi-bin/data_display_aod_v3?site=Banizoumbou&nachal=2&level=3&place_code=10.

References

- Andrews, T., Forster, P. M., & Gregory, J. M. (2009). A surface energy perspective on climate change. *Journal of Climate*, 22(10), 2557–2570. <https://doi.org/10.1175/2008JCLI2759.1>
- Avolio, E., Federico, S., Miglietta, M. M., Lo Feudo, T., Calidonna, C. R., & Sempreviva, A. M. (2017). Sensitivity analysis of WRF model PBL schemes in simulating boundary-layer variables in southern Italy: An experimental campaign. *Atmospheric Research*, 192(March), 58–71. <https://doi.org/10.1016/j.atmosres.2017.04.003>
- Berrisford, P., Dee, D., Poli, P., Brugge, R., Fiedling, K., Fuentes, M., et al. (2011). *The ERA-Interim archive, version 2.0*. Retrieved from <https://www.ecmwf.int/node/8174>
- Bouniol, D., Couvreur, F., Kamsu-Tamo, P. H., Leplay, M., Guichard, F., Favot, F., & O'connor, E. J. (2012). Diurnal and seasonal cycles of cloud occurrences, types, and radiative impact over West Africa. *Journal of Applied Meteorology and Climatology*, 51(3), 534–553. <https://doi.org/10.1175/JAMC-D-11-051.1>
- Chaibou, A. A. S., Ma, X., & Sha, T. (2020). Dust radiative forcing and its impact on surface energy budget over West Africa. *Scientific Reports*, 1–18. <https://doi.org/10.1038/s41598-020-69223-4>
- Chakraborty, T., & Lee, X. (2019). Land Cover Regulates the Spatial Variability of Temperature Response to the Direct Radiative Effect of Aerosols. *Geophysical Research Letters*, 46(15), 8995–9003. <https://doi.org/10.1029/2019GL083812>
- Chin, M., Ginoux, P., Kinne, S., Torres, O., Holben, B. N., Duncan, B. N., et al. (2002). Tropospheric Aerosol Optical Thickness from the GOCART Model and Comparisons with Satellite and Sun Photometer Measurements. *Journal of the Atmospheric Sciences*, 59, 461–483. [https://doi.org/10.1175/1520-0469\(2002\)059<0461:TAOTFT>2.0.CO;2](https://doi.org/10.1175/1520-0469(2002)059<0461:TAOTFT>2.0.CO;2)
- Curci, G., Alyuz, U., Barò, R., Bianconi, R., Bieser, J., H. Christensen, J., et al. (2019). Modelling black carbon absorption of solar radiation: Combining external and internal mixing assumptions. *Atmospheric Chemistry and Physics*, 19(1), 181–204. <https://doi.org/10.5194/acp-19-181-2019>
- Deboudt, K., Flament, P., Choël, M., Gloter, A., Sobanska, S., & Colliex, C. (2010). Mixing state of aerosols and direct observation of carbonaceous and marine coatings on African dust by individual particle analysis. *Journal of Geophysical Research Atmospheres*, 115(24), 1–14. <https://doi.org/10.1029/2010JD013921>
- Dimitrova, R., Silver, Z., Zsedrovits, T., Hocut, C. M., Leo, L. S., Di Sabatino, S., & Fernando, H. J. S. (2016). Assessment of Planetary Boundary-Layer Schemes in the Weather Research and Forecasting Mesoscale Model Using MATERHORN Field Data. *Boundary-Layer Meteorology*, 159(3), 589–609. <https://doi.org/10.1007/s10546-015-0095-8>
- Dubovik, O., Smirnov, A., Holben, B. N., King, M. D., Kaufman, Y. J., Eck, T. F., & Slutsker, I. (2000). Accuracy assessments of aerosol optical properties retrieved from AERONET sun and sky-radiance measurements. *Journal of Geophysical Research*, 105, 9791–9806.
- Engelstaedter, S., Kohfeld, K. E., Tegen, I., & Harrison, S. P. (2003). Controls of dust emissions by vegetation and topographic depressions: An evaluation using dust storm frequency data. *Geophysical Research Letters*, 30(6), 30–33. <https://doi.org/10.1029/2002GL016471>
- Evan, A. T., & Mukhopadhyay, S. (2010). African dust over the northern tropical Atlantic: 1955–2008. *Journal of Applied Meteorology and Climatology*, 49(11), 2213–2229. <https://doi.org/10.1175/2010JAMC2485.1>
- Formenti, P., Rajot, J. L., Desboeufs, K., Saïd, F., Grand, N., Chevaillier, S., & Schmechtig, C. (2011). Airborne observations of mineral dust over western Africa in the summer Monsoon season: Spatial and vertical

- variability of physico-chemical and optical properties. *Atmospheric Chemistry and Physics*, 11(13), 6387–6410. <https://doi.org/10.5194/acp-11-6387-2011>
- Gama, C., Tchepel, O., Baldasano, J. M., Basart, S., Ferreira, J., Pio, C., et al. (2015). Seasonal patterns of Saharan dust over Cape Verde - a combined approach using observations and modelling. *Tellus, Series B: Chemical and Physical Meteorology*, 67(1), 1–21. <https://doi.org/10.3402/tellusb.v67.24410>
- Ginoux, P., Chin, M., Tegen, I., Goddard, T., & In-, G. (2001). Sources and distributions of dust aerosols simulated with the GOCART model. *Journal of Geophysical Research*, 106(17), 20225–20273.
- Gkikas, A., Obiso, V., Pérez García-Pando, C., Jorba, O., Hatzianastassiou, N., Vendrell, L., et al. (2018). Direct radiative effects during intense Mediterranean desert dust outbreaks. *Atmospheric Chemistry and Physics*, 18(12), 8757–8787. <https://doi.org/10.5194/acp-18-8757-2018>
- Gu, Y., Liou, K. N., Ou, S. C., & Fovell, R. (2011). Cirrus cloud simulations using WRF with improved radiation parameterization and increased vertical resolution. *Journal of Geophysical Research Atmospheres*, 116(6), 1–14. <https://doi.org/10.1029/2010JD014574>
- Hand, V. L., Capes, G., Vaughan, D. J., Formenti, P., Haywood, J. M., & Coe, H. (2010). Evidence of internal mixing of African dust and biomass burning particles by individual particle analysis using electron beam techniques. *Journal of Geophysical Research Atmospheres*, 115(13), 1–11. <https://doi.org/10.1029/2009JD012938>
- Hansell, R. A., Tsay, S. C., Ji, Q., Hsu, N. C., Jeong, M. J., Wang, S. H., et al. (2010). An assessment of the surface longwave direct radiative effect of airborne Saharan dust during the NAMMA field campaign. *Journal of the Atmospheric Sciences*, 67(4), 1048–1065. <https://doi.org/10.1175/2009JAS3257.1>
- Haywood, J. M., Pelon, J., Formenti, P., Bharmal, N. A., Brooks, M. E., Capes, G., et al. (2008). Overview of the dust and biomass-burning experiment and African monsoon multidisciplinary analysis special observing period-0. *Journal of Geophysical Research Atmospheres*, 113(23), 1–20. <https://doi.org/10.1029/2008JD010077>
- Heinold, B., Tegen, I., Schepanski, K., Tesche, M., Esselborn, M., Freudenthaler, V., et al. (2011). Regional modelling of Saharan dust and biomass-burning smoke: Part I: Model description and evaluation. *Tellus, Series B: Chemical and Physical Meteorology*, 63(4), 781–799. <https://doi.org/10.1111/j.1600-0889.2011.00570.x>
- Hess, M., Koepke, P., & Schult, I. (1998). Optical Properties of Aerosols and Clouds: The Software Package OPAC. *Bulletin of the American Meteorological Society*, 79, 831–844. [https://doi.org/10.1175/1520-0477\(1998\)079<0831:OPOAAC>2.0.CO;2](https://doi.org/10.1175/1520-0477(1998)079<0831:OPOAAC>2.0.CO;2)
- Holben, B. N., Eck, T. F., Slutsker, I., Tanr??, D., Buis, J. P., Setzer, A., et al. (1998). AERONET - A federated instrument network and data archive for aerosol characterization. *Remote Sensing of Environment*, 66(1), 1–16. [https://doi.org/10.1016/S0034-4257\(98\)00031-5](https://doi.org/10.1016/S0034-4257(98)00031-5)
- Huang, J., Fu, Q., Su, J., Tang, Q., Minnis, P., Hu, Y., et al. (2009). Taklimakan dust aerosol radiative heating derived from CALIPSO observations using the Fu-Liou radiation model with CERES constraints. *Atmospheric Chemistry and Physics*, 9(12), 4011–4021. <https://doi.org/10.5194/acp-9-4011-2009>
- Huang, J., Yu, H., Dai, A., Wei, Y., & Kang, L. (2017). Drylands face potential threat under 2 °C global warming target. *Nature Climate Change*, 7(6), 417–422. <https://doi.org/10.1038/nclimate3275>
- IPCC. (2021). *Climate Change 2021: The Physical Science Basis. Contribution of Working Group I to the Sixth Assessment Report of the Intergovernmental Panel on Climate Change*. Cambridge, United Kingdom.
- Johnson, B. T., Osborne, S. R., Haywood, J. M., & Harrison, M. A. J. (2008). Aircraft measurements of biomass burning aerosol over West Africa during DABEX. *Journal of Geophysical Research*, 113, D00C06. <https://doi.org/10.1029/2007JD009451>
- Johnson, B. T., Heese, B., McFarlane, S. a., Chazette, P., Jones, A., & Bellouin, N. (2008). Vertical distribution and radiative effects of mineral dust and biomass burning aerosol over West Africa during DABEX. *Journal of Geophysical Research*, 113, 1–16. <https://doi.org/10.1029/2008JD009848>
- Keeler, E., Ritsche, M., & Kyrouac, J. (2006). Balloon-Borne Sounding System (SONDEWNP). [Dataset]

Atmospheric Radiation Measurement (ARM) User Facility. ARM Data Center.
<https://doi.org/10.5439/1021460>

- Kleczek, M. A., Steeneveld, G. J., & Holtslag, A. A. M. (2014). Evaluation of the Weather Research and Forecasting Mesoscale Model for GABLS3: Impact of Boundary-Layer Schemes, Boundary Conditions and Spin-Up. *Boundary-Layer Meteorology*, *152*(2), 213–243. <https://doi.org/10.1007/s10546-014-9925-3>
- Kyrouac, J., & Shi, Y. (2005). Surface Meteorological Instrumentation (MET). [Dataset] *Atmospheric Radiation Measurement (ARM) User Facility*. ARM Data Center. <https://doi.org/10.5439/1786358>
- Lau, K. M., & Kim, K. M. (2007). Cooling of the Atlantic by Saharan dust. *Geophysical Research Letters*, *34*(23), 8–11. <https://doi.org/10.1029/2007GL031538>
- Li, Z., Guo, J., Ding, A., Liao, H., Liu, J., Sun, Y., et al. (2017). Aerosol and boundary-layer interactions and impact on air quality. *National Science Review*, *4*(6), 810–833. <https://doi.org/10.1093/nsr/nwx117>
- Lou, M., Guo, J., Wang, L., Xu, H., Chen, D., Miao, Y., et al. (2019). On the Relationship Between Aerosol and Boundary Layer Height in Summer in China Under Different Thermodynamic Conditions. *Earth and Space Science*, *6*(5), 887–901. <https://doi.org/10.1029/2019EA000620>
- McNider, R. T., Steeneveld, G. J., Holtslag, A. A. M., Pielke, R. A., Mackaro, S., Pour-Biazar, A., et al. (2012). Response and sensitivity of the nocturnal boundary layer over land to added longwave radiative forcing. *Journal of Geophysical Research: Atmospheres*, *117*(D14), n/a-n/a. <https://doi.org/10.1029/2012jd017578>
- Meloni, D., Junkermann, W., di Sarra, A., Cacciani, M., De Silvestri, L., Di Iorio, T., et al. (2015). Altitude-resolved shortwave and longwave radiative effects of desert dust in the Mediterranean during the GAMARF campaign: Indications of a net daily cooling in the dust layer. *Journal of Geophysical Research: Atmospheres*, *120*, 3386–3407. <https://doi.org/10.1002/2014JD022312>
- Miller, M. A., & Slingo, A. (2007). Measuring Radiative Flux Divergence in West Africa. *Bulletin of the American Meteorological Society*, (August), 1229–1244. <https://doi.org/10.1175/BAMS-88-8-1229>
- Nair, U. S., McNider, R., Patadia, F., Christopher, S. a., & Fuller, K. (2011). Sensitivity of nocturnal boundary layer temperature to tropospheric aerosol surface radiative forcing under clear-sky conditions. *Journal of Geophysical Research: Atmospheres*, *116*, 1–16. <https://doi.org/10.1029/2010JD014068>
- Patadia, F., Yang, E. S., & Christopher, S. A. (2009). Does dust change the clear sky top of atmosphere shortwave flux over high surface reflectance regions? *Geophysical Research Letters*, *36*(15), 1–5. <https://doi.org/10.1029/2009GL039092>
- Pinker, R. T., Liu, H., Osborne, S. R., & Akoshile, C. (2010). Radiative effects of aerosols in sub-Sahel Africa: Dust and biomass burning. *Journal of Geophysical Research Atmospheres*, *115*(15), 1–15. <https://doi.org/10.1029/2009JD013335>
- Prospero, J. M., & Mayol-Bracero, O. L. (2013). Understanding the Transport and Impact of African Dust on the Caribbean Basin. *Bulletin of the American Meteorological Society*, *94*(9), 1329–1337. <https://doi.org/10.1175/BAMS-D-12-00142.1>
- Rohde, R., Muller, R. A., Jacobsen, R., Muller, E., Perlmutter, S., Rosenfeld, A., et al. (2013). A new estimate of the average Earth surface land temperature spanning 1753 to 2011. *Geoinformatics and Geostatistics: An Overview*, *1*(1), 2. <https://doi.org/10.4172/2327-4581.1000101>
- Scarnato, B. V., China, S., Nielsen, K., & Mazzoleni, C. (2015). Perturbations of the optical properties of mineral dust particles by mixing with black carbon: A numerical simulation study. *Atmospheric Chemistry and Physics*, *15*(12), 6913–6928. <https://doi.org/10.5194/acp-15-6913-2015>
- Sengupta, M., Andreas, A., Dooraghi, M., Habte, A., Kutchenreiter, M., Reda, I., et al. (2005a). Ground Radiometers on Stand for Upwelling Radiation (GNDRAD60S). *Atmospheric Radiation Measurement (ARM) User Facility*. [Dataset] ARM Data Center. <https://doi.org/10.5439/1025192>
- Sengupta, M., Andreas, A., Dooraghi, M., Habte, A., Kutchenreiter, M., Reda, I., et al. (2005b). Sky Radiometers on Stand for Downwelling Radiation (SKYRAD60S). [Dataset] *Atmospheric Radiation Measurement (ARM) User Facility*. ARM Data Center. <https://doi.org/10.5439/1025281>

- Skamarock, W. C., Klemp, J. B., Dudhi, J., Gill, D. O., Barker, D. M., Duda, M. G., et al. (2008). *A Description of the Advanced Research WRF Version 3*. [Software] *NCAR Technical Note*. <https://doi.org/10.5065/D6DZ069T>
- Slingo, A., White, H. E., Bharmal, N. A., & Robinson, G. J. (2009). Overview of observations from the RADAGAST experiment in Niamey, Niger: 2. Radiative fluxes and divergences. *Journal of Geophysical Research Atmospheres*, *114*(13), 1–19. <https://doi.org/10.1029/2008JD010497>
- Slingo, A., Bharmal, N. A., Robinson, G. J., Settle, J. J., Allan, R. P., White, H. E., et al. (2009). Overview of observations from the RADAGAST experiment in Niamey, Niger: Meteorology and thermodynamic variables. *Journal of Geophysical Research Atmospheres*, *114*(13), 1–18. <https://doi.org/10.1029/2008JD009909>
- Solmon, F., Elguindi, N., Mallet, M., Flamant, C., & Formenti, P. (2021). West African monsoon precipitation impacted by the South Eastern Atlantic biomass burning aerosol outflow. *Npj Climate and Atmospheric Science*, *4*(1), 1–7. <https://doi.org/10.1038/s41612-021-00210-w>
- Sridhar, V., Elliott, R. L., Chen, F., & Brotzge, J. A. (2002). Validation of the NOAA-OSU land surface model using surface flux measurements in Oklahoma. *Journal of Geophysical Research Atmospheres*, *107*(20). <https://doi.org/10.1029/2001JD001306>
- Sullivan, R., Billesbach, D., Keeler, E., & Ermold, B. (2005). Eddy Correlation Flux Measurement System (30ECOR). [Dataset] *Atmospheric Radiation Measurement (ARM) User Facility*. ARM Data Center. <https://doi.org/10.5439/1025039>
- Sun, X., Holmes, H. A., Osibanjo, O. O., Sun, Y., & Ivey, C. E. (2017). Evaluation of surface fluxes in the WRF model: Case study for farmland in rolling terrain. *Atmosphere*, *8*(10), 1–23. <https://doi.org/10.3390/atmos8100197>
- Tanaka, T. Y., & Chiba, M. (2006). A numerical study of the contributions of dust source regions to the global dust budget. *Global and Planetary Change*, *52*(1–4), 88–104. <https://doi.org/10.1016/j.gloplacha.2006.02.002>
- Tanre, D., & Rajot, J. L. (2022). Banizoumbou AERONET. NASA. [Dataset] Retrieved from https://aeronet.gsfc.nasa.gov/cgi-bin/data_display_aod_v3?site=Banizoumbou&nachal=2&level=3&place_code=10
- Tsikerdekis, A., Zanis, P., Georgoulas, A. K., Alexandri, G., Katragkou, E., Karacostas, T., & Solmon, F. (2019). Direct and semi-direct radiative effect of North African dust in present and future regional climate simulations. *Climate Dynamics*, *53*(7–8), 4311–4336. <https://doi.org/10.1007/s00382-019-04788-z>
- Tuccella, P., Curci, G., Pitari, G., Lee, S., & Jo, D. S. (2020). Direct Radiative Effect of Absorbing Aerosols: Sensitivity to Mixing State, Brown Carbon, and Soil Dust Refractive Index and Shape. *Journal of Geophysical Research: Atmospheres*, *125*(2), 1–25. <https://doi.org/10.1029/2019JD030967>
- Walters, J. T., McNider, R. T., Shi, X., Norris, W. B., & Christy, J. R. (2007). Positive surface temperature feedback in the stable nocturnal boundary layer. *Geophysical Research Letters*, *34*, 1–5. <https://doi.org/10.1029/2007GL029505>
- Warner, T. T. (2011). *Numerical Weather and Climate Prediction* (1st ed.). Cambridge, United Kingdom: Cambridge University Press.
- Wei, L., Wang, Y., Liu, S., Zhang, G. J., & Wang, B. (2021). Distinct roles of land cover in regulating spatial variabilities of temperature responses to radiative effects of aerosols and clouds. *Environmental Research Letters*, *16*(12). <https://doi.org/10.1088/1748-9326/ac3f04>
- Van Der Werf, G. R., Randerson, J. T., Giglio, L., Collatz, G. J., Kasibhatla, P. S., & Arellano, A. F. (2006). Interannual variability in global biomass burning emissions from 1997 to 2004. *Atmospheric Chemistry and Physics*, *6*(11), 3423–3441. <https://doi.org/10.5194/acp-6-3423-2006>
- Yoshioka, M., Mahowald, N. M., Conley, A. J., Collins, W. D., Fillmore, D. W., Zender, C. S., & Coleman, D. B. (2007). Impact of Desert Dust Radiative Forcing on Sahel Precipitation: Relative Importance of Dust Compared to Sea Surface Temperature Variations, Vegetation Changes, and Greenhouse Gas Warming. *Journal of Climate*, *20*, 1445–1467. <https://doi.org/10.1175/JCLI4056.1>
- Zhou, L. (2016). Desert Amplification in a Warming Climate. *Scientific Reports*, *6*(August), 1–13.

<https://doi.org/10.1038/srep31065>

Zhou, L., Dickinson, R. E., Tian, Y., Vose, R. S., & Dai, Y. (2007). Impact of vegetation removal and soil aridation on diurnal temperature range in a semiarid region: application to the Sahel. *Proceedings of the National Academy of Sciences of the United States of America*, *104*(46), 17937–17942. <https://doi.org/10.1073/pnas.0700290104>

Zhou, L., Dickinson, R., Dirmeyer, P., Chen, H., Dai, Y., & Tian, Y. (2008). Asymmetric response of maximum and minimum temperatures to soil emissivity change over the Northern African Sahel in a GCM. *Geophysical Research Letters*, *35*(5). <https://doi.org/10.1029/2007GL032953>

Zhou, L., Dickinson, R. E., Dai, A., & Dirmeyer, P. (2010). Detection and attribution of anthropogenic forcing to diurnal temperature range changes from 1950 to 1999: Comparing multi-model simulations with observations. *Climate Dynamics*, *35*(7), 1289–1307. <https://doi.org/10.1007/s00382-009-0644-2>

Accepted Article

Figures

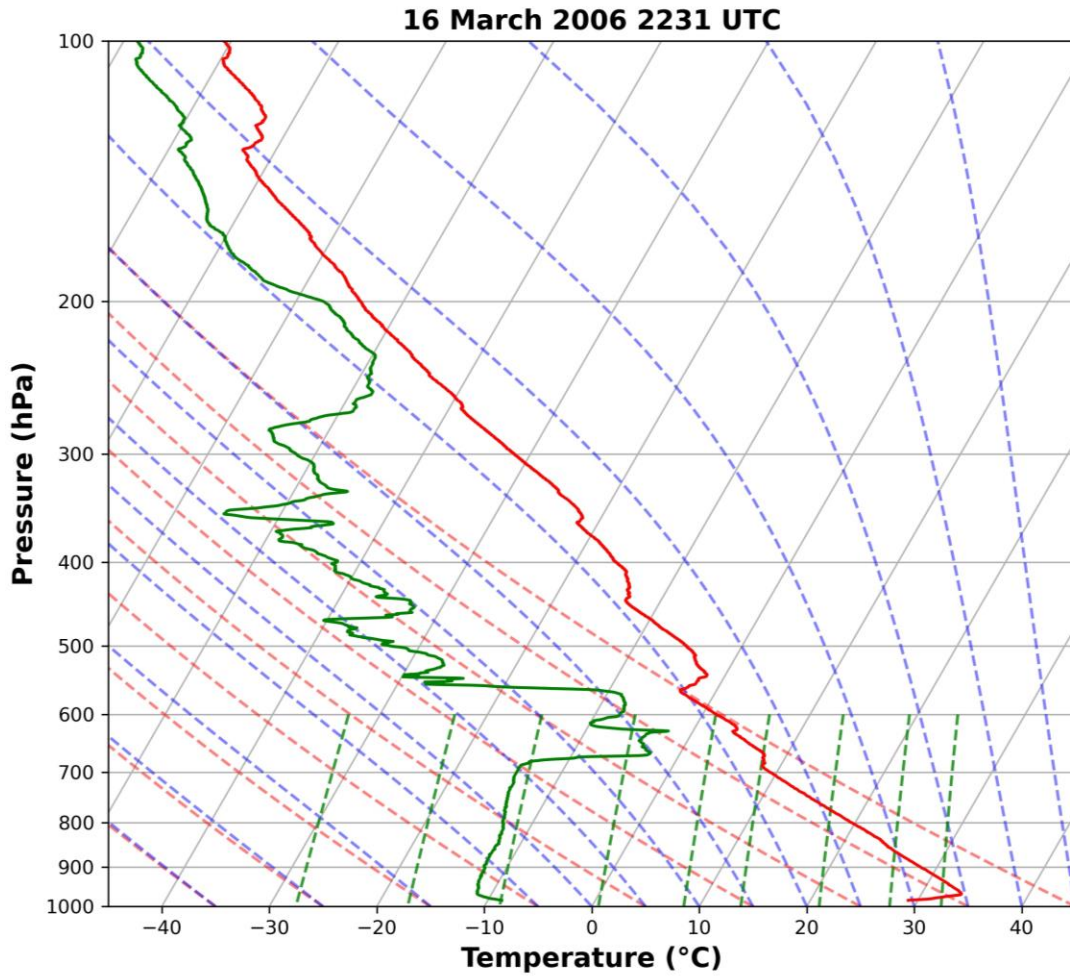


Figure 1. Initial temperature (red) and dewpoint (green) profile for the 17 March 2006 case day plotted on a Skew-T Log-P diagram. Title indicates sounding launch time. Sounding times vary for each case but are always within 1.5 hours of 0000 UTC, the simulation start time.

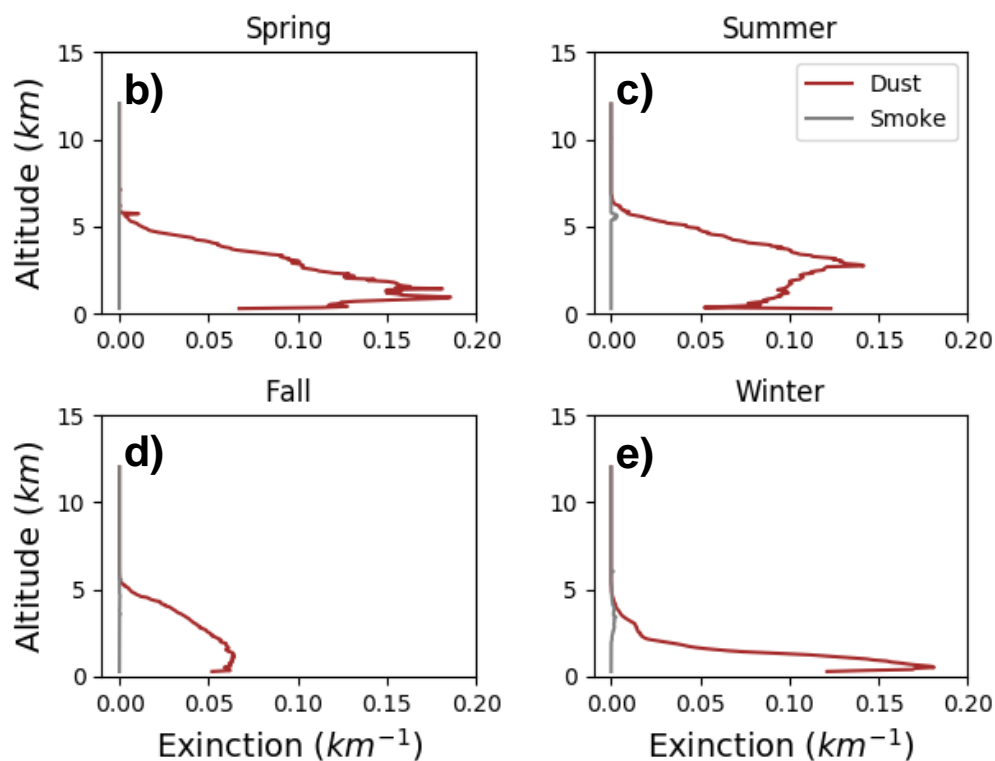
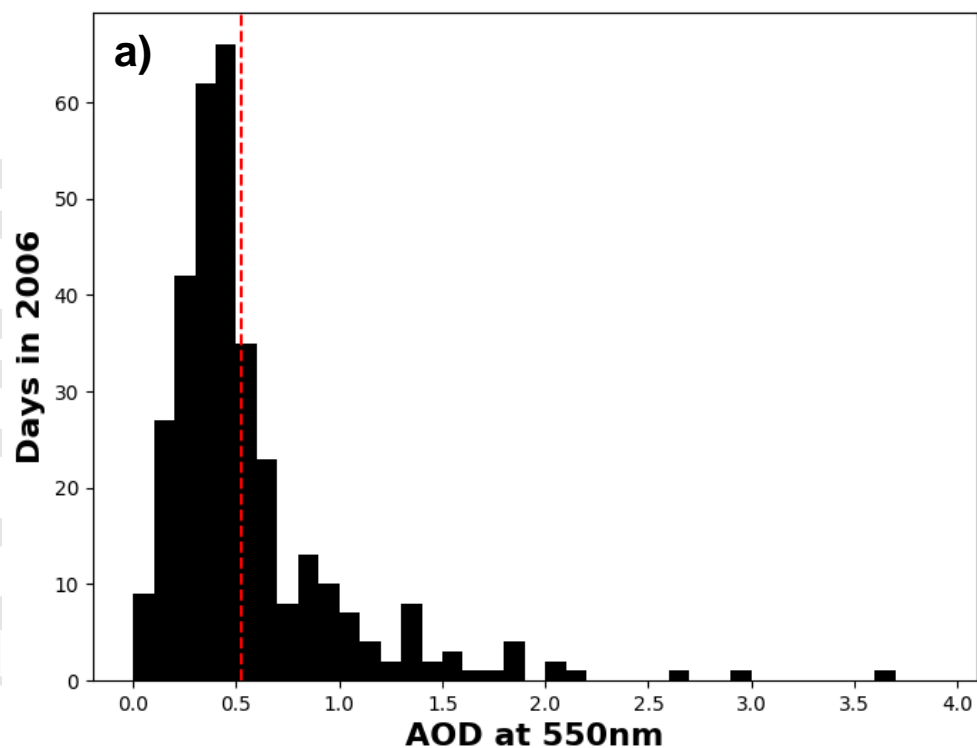


Figure 2. (a) Distribution of AOD at the Banizoumbou, Niger AeRoNet station in 2006. Dashed line depicts mean AOD. (b-e) Vertical distribution of aerosol optical extinction coefficient for dust and smoke aerosols. To construct the seasonal profiles, CALIPSO nighttime retrievals over Niger were average for the period 2007-2015 and grouped by season. (b) Spring (MAM), (c) Summer (JJA), (d) Fall (SON), and (e) Winter (DJF) are considered.

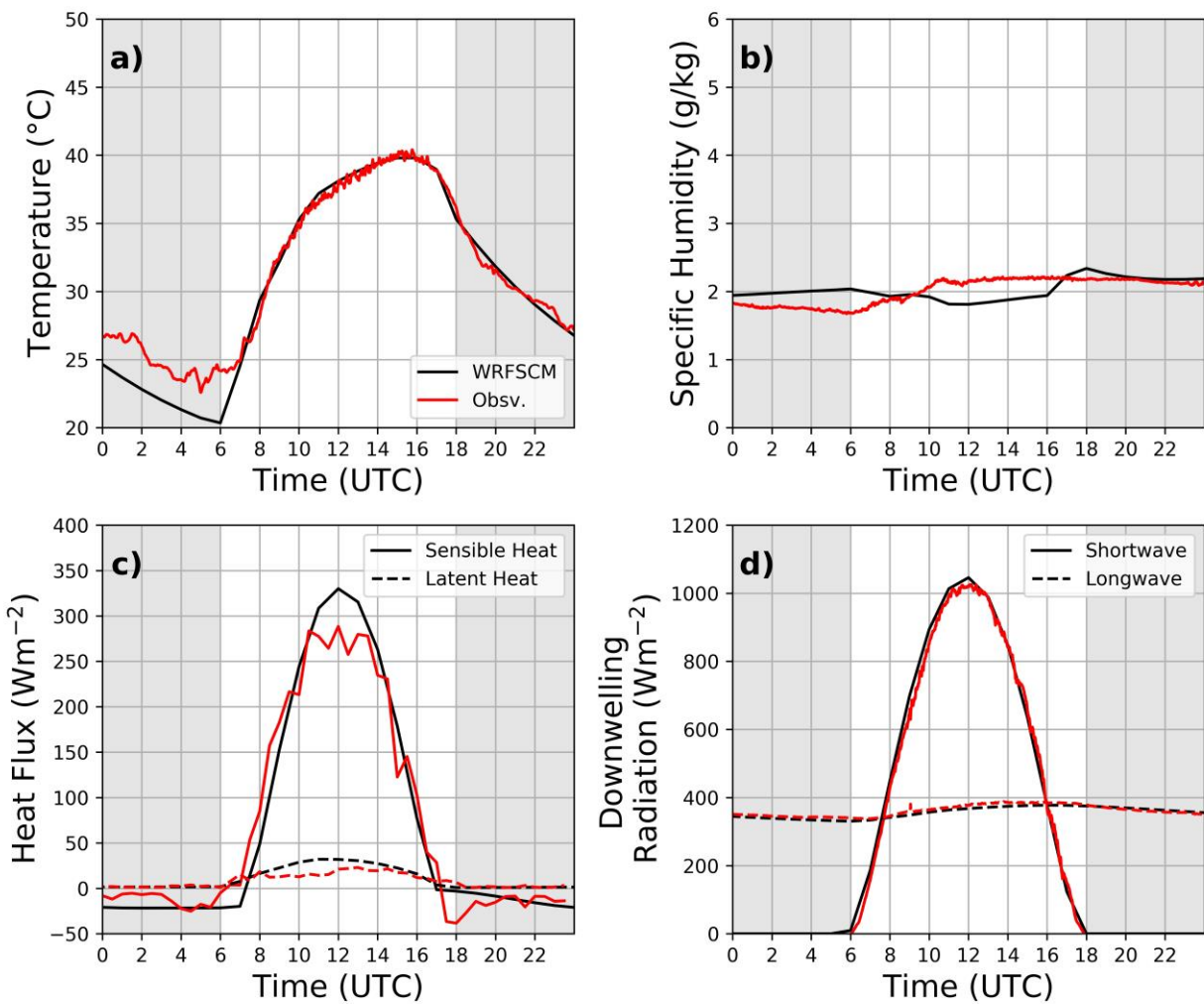


Figure 3. Comparison of observed (red) and Control simulation (black) near-surface (a) temperature, (b) specific humidity, (c) heat fluxes, and (d) downwelling radiation for the case day of 17 March 2006. Shaded region is nighttime.

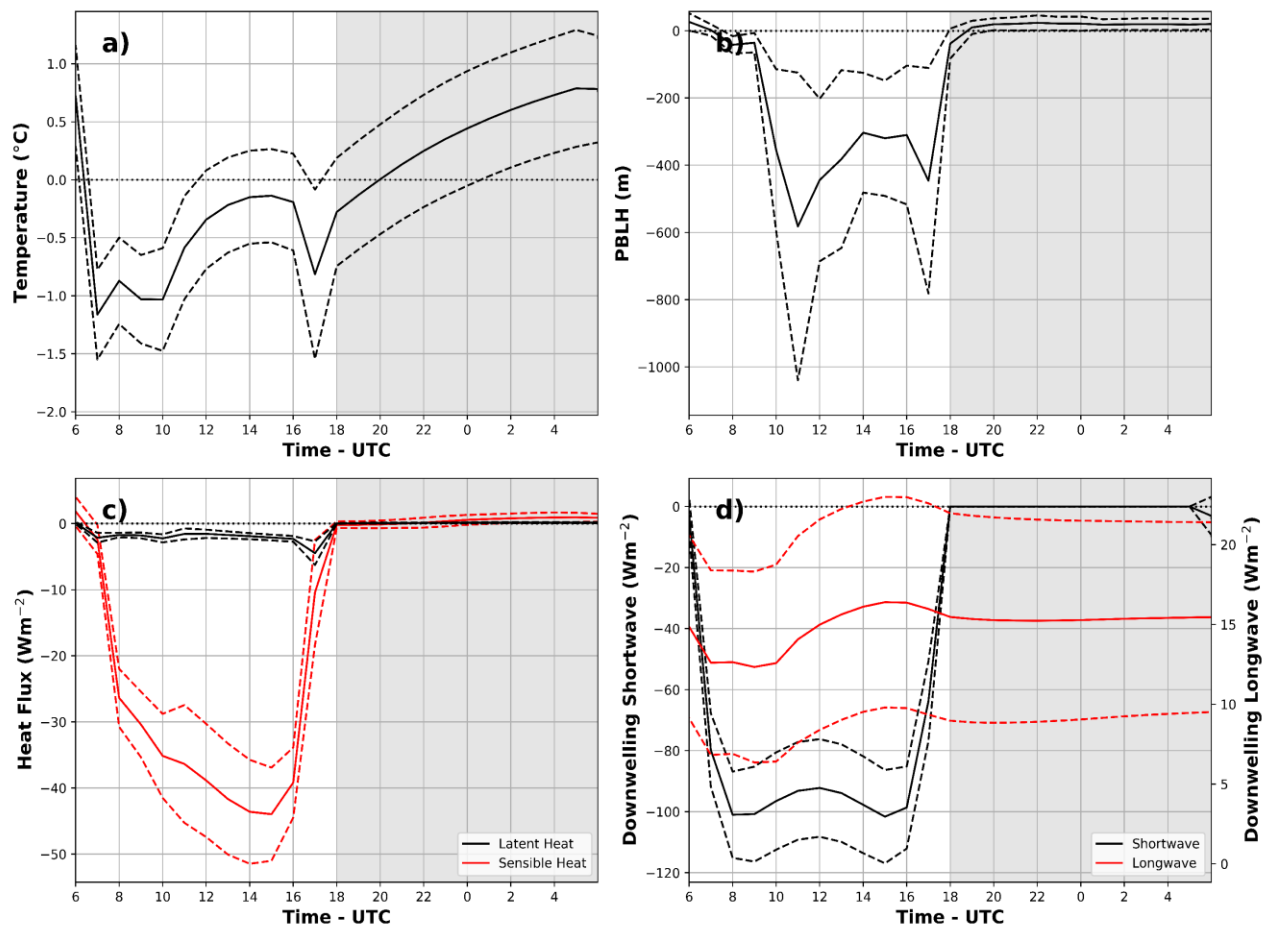


Figure 4. Mean differences between the control and aerosol free experiments using the DABEX aerosol loading profiles. The difference is taken as control minus aerosol free. Dashed envelopes are one standard deviation above and below the mean. Shaded region is nighttime.

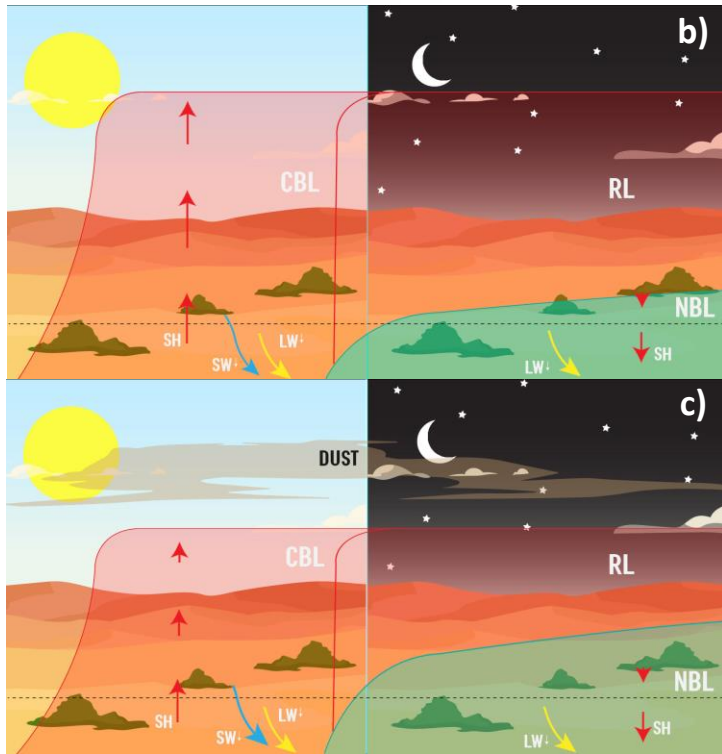
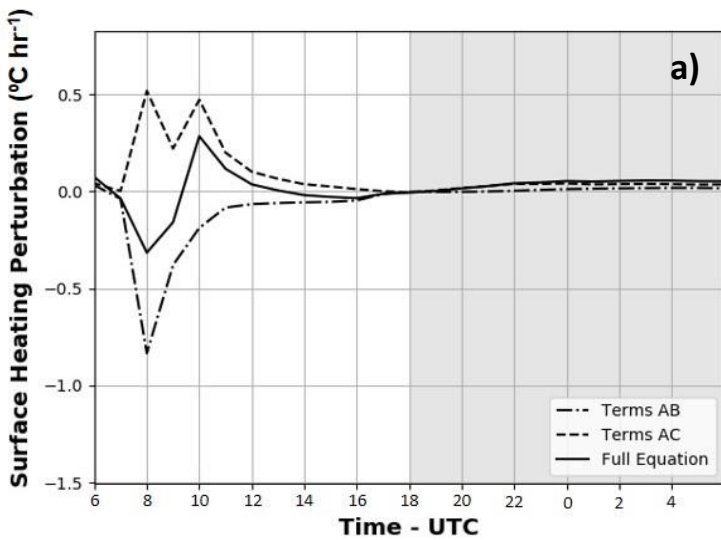


Figure 5. (a) Evolution of temperature tendency due to changes in surface sensible heat flux (Term AB) and boundary layer height (Term AC). Differences are taken as control minus aerosol free. (b) Conceptual diagram of boundary layer evolution under clear sky conditions. During the day, near-surface heat fluxes are directed upward, warming the atmosphere. During the night near-surface heat fluxes are directed downward, cooling the atmosphere. (c) Conceptual diagram showing the impact of dust on boundary layer evolution compared to the clear sky scenario. Dust radiative forcing reduces daytime boundary layer depth, but deepens the nocturnal boundary layer through addition of downwelling longwave radiation. The reduced boundary layer depth during daytime increases flux convergence, producing a surface warming tendency that partially offsets daytime cooling. The greater nocturnal boundary layer depth reduces near-surface heat flux divergence, slowing the rate of atmospheric cooling. CBL is convective boundary layer, RL is Remnant Layer; NBL is nocturnal boundary layer; SH is sensible heat flux; SW is shortwave radiative flux; and LW is longwave radiative flux.

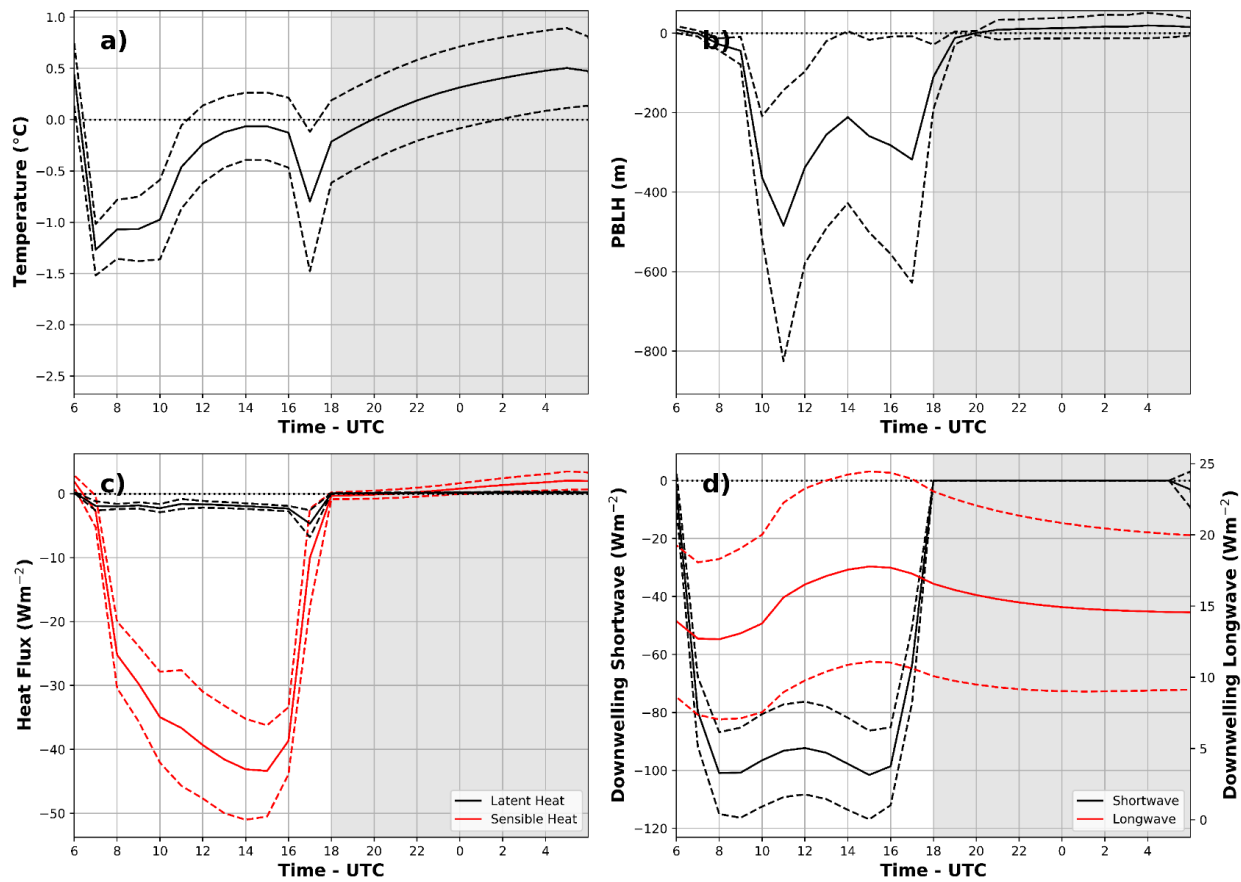


Figure 6. Mean differences between the aerosol free and control experiments with 18 vertical levels using the DABEX aerosol loading profiles. The difference is taken as experimental minus control. Dashed envelopes are one standard deviation above and below the mean. Shaded region is nighttime.

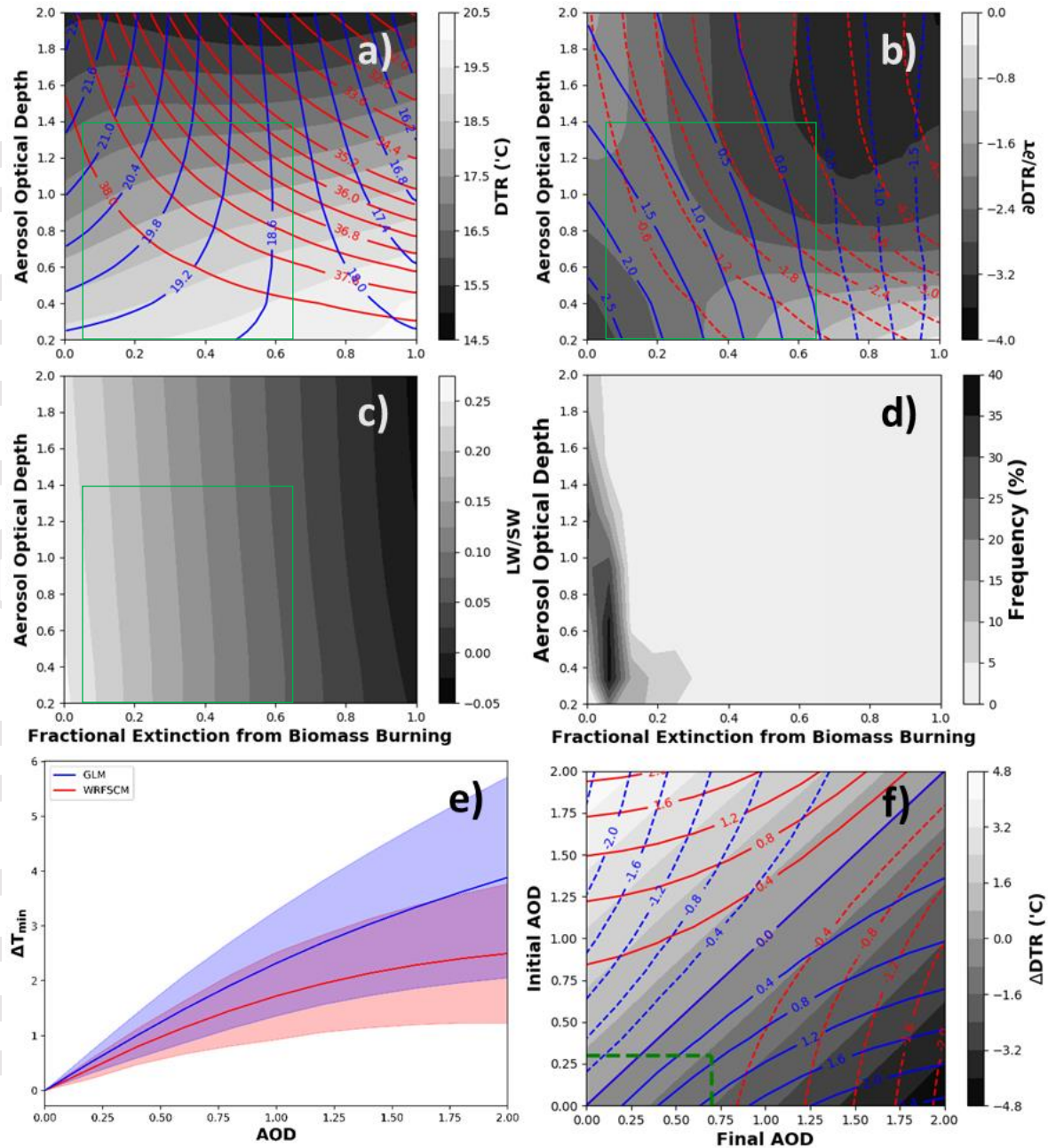


Figure 7. (a) Contours of mean DTR (shaded), mean T_{\max} (red), and mean T_{\min} (blue) with respect to AOD and AE. Means are taken from the aerosol sensitivity experiments. The green box corresponds to observed AOD and f_{bb} . (b) Sensitivity of T_{\max} (red), T_{\min} (blue), and DTR (shading) to aerosol AOD as a function of AOD and composition. (c) Ratio of longwave to shortwave radiative forcing by aerosols. Positive values indicate longwave forcing offsets shortwave forcing. (d) Frequency of aerosol loading and composition scenarios during 2006. (e) Mean predicted change in T_{\min} relative to aerosol-free conditions for the GLM and WRFSCM. Shading indicates two standard deviations from the mean. (f) Contours of change in T_{\min} (blue), T_{\max} (red), and DTR (shaded) with change in AOD, $f_{\text{bb}} = 0.22$ (observed mean), and aerosol loading profile determined by DABEX. To estimate change in temperature, draw a line from the initial AOD across and a line from the final AOD up. Contour values at the intersection are the change in temperature. Green lines demonstrate how 1950-1980 LDA increased AOD from mean 0.3-0.7, warming T_{\min} by approximately 0.6°C .

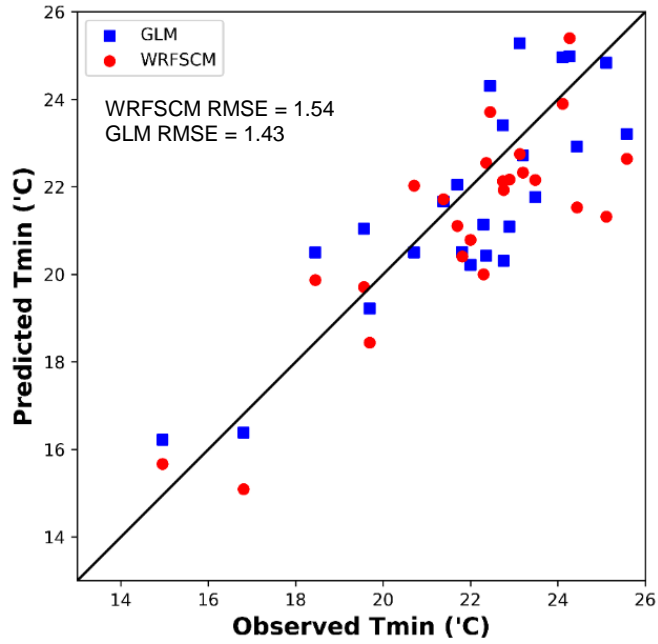


Figure 8. Accuracy of General Linear Model and WRFSCM compared to observed T_{min}. Black line is perfect predictive power.

Tables

Table 1. WRFSCM physics parameterizations.

Microphysics Scheme	None
Cumulus Scheme	None
Surface Layer Scheme	Revised MM5
Surface Scheme	NOAH
Boundary Layer Scheme	YSU
SW and LW Radiation	FLG

Table 2. Case days used in study. Star indicates inclusion in Aerosol Sensitivity Experiments.

10 Jan 2006*	22 Feb 2006	6 March 2006	7 Nov 2006
6 Feb 2006	23 Feb 2006	15 March 2006	9 Nov 2006*
12 Feb 2006	28 Feb 2006	17 March 2006*	12 Nov 2006
14 Feb 2006*	1 March 2006	27 March 2006*	16 Nov 2006
20 Feb 2006	3 March 2006	28 March 2006	6 Dec 2006*
21 Feb 2006	4 March 2006*	10 April 2006*	7 Dec 2006

Table 3. Summary of each WRF SCM experiment.

Experiment	Description
Control	Daily observed sounding conditions, Observed aerosols with DABEX vertical distribution
Aerosol Free	Daily observed sounding conditions, No aerosols
Model Resolution	Control and aerosol free but with 18 vertical levels instead of 60.
Vertical Distribution	Observed soundings and aerosols but with seasonal CALIPSO vertical distribution
Aerosol sensitivity	Subset of 8 case days with arbitrary aerosol mixtures and DABEX vertical distribution

Table 4. OPAC aerosol mixture used for biomass burning smoke and corresponding optical properties. Note concentrations are later scaled by AOD in the WRFSCM.

Water Soluble (cm ⁻³)	Soot (cm ⁻³)	ω_0	g	k_{ext} (m ² g ⁻¹)	AE
1200	3600	0.818	0.654	3.688	1.56

Table 5. Change in Akaike Information Criterion (AIC) as each variable is added to the GLM. Rows are added sequentially to the GLM with decrease in AIC indicating model improvement.

Variable	ΔAIC
+Season	-240.21
+Mixing Ratio	-148.17
+Tmax	-152.14
+AOD	-28.07
+Mixing Ratio:AOD	-6.29
+Season:AOD	-6.24
+Mixing Ratio:Tmax	-4.13
+Mixing Ratio:Season	-14.39

Table 6. Mean impact of aerosols on temperature in the vertical distribution experiments. Paired Student's t-test used to calculate significance. Note that, when vertical distribution is specified based on CALIPSO climatology, aerosol layers tend to be located at higher altitudes compared to in-situ aircraft observations. This reduces downwelling longwave radiation at the surface, especially in the afternoon and causes more cooling during daytime and less warming during nighttime.

	ΔT_{min}	ΔT_{max}	ΔDTR	$p_{T_{\text{min}}}$	$p_{T_{\text{max}}}$	p_{DTR}
Control	0.73 ± 0.09	-0.14 ± 0.08	-0.88 ± 0.05	< 0.001	< 0.050	< 0.001
Spring	0.59 ± 0.09	-0.21 ± 0.09	-0.81 ± 0.05	< 0.001	< 0.050	< 0.001
Summer	0.47 ± 0.09	-0.56 ± 0.11	-1.03 ± 0.05	< 0.001	< 0.001	< 0.001
Fall	0.56 ± 0.09	-0.48 ± 0.11	-1.04 ± 0.04	< 0.001	< 0.001	< 0.001
Winter	0.61 ± 0.09	-0.50 ± 0.10	-1.11 ± 0.05	< 0.001	< 0.001	< 0.001

Figures

Figure 1. Initial temperature (red) and dewpoint (green) profile for the 17 March 2006 case day plotted on a Skew-T Log-P diagram. Title indicates sounding launch time. Sounding times vary for each case but are always within 1.5 hours of 0000 UTC, the simulation start time.

Figure 2. (a) Distribution of AOD at the Banizoumbou, Niger AeRoNet station in 2006. Dashed line depicts mean AOD. (b-e) Vertical distribution of aerosol optical extinction coefficient for dust and smoke aerosols. To construct the seasonal profiles, CALIPSO nighttime retrievals over Niger were average for the period 2007-2015 and grouped by season. (b) Spring (MAM), (c) Summer (JJA), (d) Fall (SON), and (e) Winter (DJF) are considered.

Figure 3. Comparison of observed (red) and Control simulation (black) near-surface (a) temperature, (b) specific humidity, (c) heat fluxes, and (d) downwelling radiation for the case day of 17 March 2006. Shaded region is nighttime.

Figure 4. Mean differences between the control and aerosol free experiments using the DABEX aerosol loading profiles. The difference is taken as control minus aerosol free. Dashed envelopes are one standard deviation above and below the mean. Shaded region is nighttime.

Figure 5. (a) Evolution of temperature tendency due to changes in surface sensible heat flux (Term AB) and boundary layer height (Term AC). Differences are taken as control minus aerosol free. (b) Conceptual diagram of boundary layer evolution under clear sky conditions. During the day, near-surface heat fluxes are directed upward, warming the atmosphere. During the night near-surface heat fluxes are directed downward, cooling the atmosphere. (c) Conceptual diagram showing the impact of dust on boundary layer evolution compared to the clear sky scenario. Dust radiative forcing reduces daytime boundary layer depth, but deepens the nocturnal boundary layer through addition of downwelling longwave radiation. The reduced boundary layer depth during daytime increases flux convergence, producing a surface warming tendency that partially offsets daytime cooling. The greater nocturnal boundary layer depth reduces near-surface heat flux divergence, slowing the rate of atmospheric cooling. CBL is convective boundary layer; RL is Remnant Layer; NBL is nocturnal boundary layer; SH is sensible heat flux; SW is shortwave radiative flux; and LW is longwave radiative flux.

Figure 6. Mean differences between the aerosol free and control experiments with 18 vertical levels using the DABEX aerosol loading profiles. The difference is taken as experimental minus control. Dashed envelopes are one standard deviation above and below the mean. Shaded region is nighttime.

Figure 7. (a) Contours of mean DTR (shaded), mean T_{\max} (red), and mean T_{\min} (blue) with respect to AOD and AE. Means are taken from the aerosol sensitivity experiments. The green box corresponds to observed AOD and f_{bb} . (b) Sensitivity of T_{\max} (red), T_{\min} (blue), and DTR (shading) to aerosol AOD as a function of AOD and composition. (c) Ratio of longwave to shortwave radiative forcing by aerosols. Positive values indicate longwave forcing offsets shortwave forcing. (d) Frequency of aerosol loading and composition scenarios during 2006. (e) Mean predicted change in T_{\min} relative to aerosol-free conditions for the GLM and WRFSCM. Shading indicates two standard deviations from the mean. (f) Contours of change in T_{\min} (blue), T_{\max} (red), and DTR (shaded) with change in AOD, $f_{\text{bb}} = 0.22$ (observed mean), and aerosol loading profile determined by DABEX. To estimate change in temperature, draw a line from the initial AOD across and a line from the final AOD up. Contour values at the intersection are the change in temperature. Green lines demonstrate how 1950-1980 LDA increased AOD from mean 0.3-0.7, warming T_{\min} by approximately 0.6 °C.

Figure 8. Accuracy of General Linear Model and WRFSCM compared to observed T_{\min} . Black line is perfect predictive power.

Tables

Table 1. WRFSCM physics parameterizations.

Table 2. Case days used in study. Star indicates inclusion in Aerosol Sensitivity Experiments.

Table 3. Summary of each WRF SCM experiment.

Table 4. OPAC aerosol mixture used for biomass burning smoke and corresponding optical properties. Note concentrations are later scaled by AOD in the WRFSCM.

Table 5. Change in Akaike Information Criterion (AIC) as each variable is added to the GLM. Rows are added sequentially to the GLM with decrease in AIC indicating model improvement.

Table 6. Mean impact of aerosols on temperature in the vertical distribution experiments. Paired Student's t-test used to calculate significance. Note that, when vertical distribution is specified based on CALIPSO climatology, aerosol layers tend to be located at higher altitudes compared to in-situ aircraft observations. This reduces downwelling longwave radiation at the surface, especially in the afternoon and causes more cooling during daytime and less warming during nighttime.

Accepted Article